



Research Article

Enhanced Long-term Stability and Carbon Resistance of Ni/Mn_xO_y-Al₂O₃ Catalyst in Near-equilibrium CO₂ Reforming of Methane for Syngas Production

Baya Djebbari¹, Fouzia Touahra^{2,*}, Nadia Aider⁴, Ferroudja Bali³, Moussa Sehalia², Redouane Chebout², Khaldoun Bachari², Djamila Halliche³

¹Department of Chemistry, Faculty of sciences, University of M'hamed Bougara, Independence Avenue, 35000 Boumerdes, Algeria.

²Centre de Recherche Scientifique et Technique en Analyses Physico-chimiques (CRAPC), BP 384-Bou-Ismaïl-RP42004, Tipaza, Algeria.

³Laboratory of Natural Gas Chemistry, Faculty of Chemistry, University of Science and Technology Houari Boumediene, BP 32 16111 Algiers, Algeria.

⁴Département de Chimie, Faculté des Sciences, University Mouloud Memmeri of Tizi ousou, Tizi-ousou, Algérie.

Received: 1st January 2020; Revised: 6th March 2020; Accepted: 13th March 2020;
Available online: 30th July 2020; Published regularly: August 2020

Abstract

Herein we study the catalytic activity/stability of a new generation of cheap and readily available Ni and Al-based catalysts using two Mn precursors, namely Mn(NO₃)₂ and Mn(EDTA)²⁻ complex in the reaction of CO₂ reforming of methane. In this respect, Ni/Al₂O₃ and two types of Ni/Mn_xO_y-Al₂O₃ catalysts were successfully synthesized and characterized using various analytical techniques: TGA, ICP, XRD, BET, FTIR, TPR-H₂, SEM-EDX, TEM, XPS, and TPO-O₂. Utilization of Mn(EDTA)²⁻ as synthetic precursor successfully furnished Ni/Al₂O₃-Mn_xO_yY (Y = EDTA) catalyst which was more active during CO₂ reforming of methane when compared to Ni/Mn_xO_y-Al₂O₃ catalyst, synthesized using Mn(NO₃)₂ precursor. Compared to Ni/Mn_xO_y-Al₂O₃, Ni/Al₂O₃-Mn_xO_yY catalyst afforded near-equilibrium conversion values at 700 °C (ca. 95% conversion for CH₄ and CO₂, and H₂/CO = 0.99 over 50 h reaction time). Also, Ni/Al₂O₃-Mn_xO_yY showed more resistance to carbon formation and sintering; interestingly, after 50 h reaction time, the size of Ni⁰ particles in Ni/Mn_xO_y-Al₂O₃ almost doubled while that of Ni/Al₂O₃-Mn_xO_yY remained unchanged. The elevated conversion of CO₂ and CH₄ in conjunction with the observed low carbon deposition on the surface of our best catalyst (Ni/Al₂O₃-Mn_xO_yY) indicated the presence of Mn_xO_y oxide positioning mediated simultaneous *in-situ* carbon elimination with subsequent generation of oxygen vacant sites on the surface for more CO₂ adsorption. Copyright © 2020 BCREC Group. All rights reserved

Keywords: Mn_xO_y; Al₂O₃; CO₂ reforming of methane; carbon resistance

How to Cite: Djebbari, B., Touahra, F., Aider, N., Bali, F., Sehalia, M., Chebout, R., Bachari, K., Halliche, D. (2020). Enhanced Long-term Stability and Carbon Resistance of Ni/Mn_xO_y-Al₂O₃ Catalyst in Near-equilibrium CO₂ Reforming of Methane for Syngas Production. *Bulletin of Chemical Reaction Engineering & Catalysis*, 15(2), 331-347 (doi:10.9767/bcrec.15.2.6983.331-347)

Permalink/DOI: <https://doi.org/10.9767/bcrec.15.2.6983.331-347>

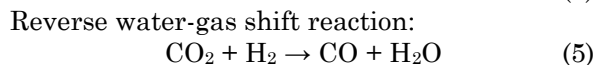
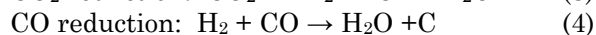
1. Introduction

Global warming is one of the major environmental challenges of our time. A major cause of

the current global warming trend is the increase in the amount of greenhouse gas released to our environment (CH₄ and CO₂). Therefore, finding new ways to help tackle and/or reduce the level of greenhouse gas is of paramount importance, this could be achieved by either increasing the

* Corresponding Author.
E-mail: tfafaze256@yahoo.fr (F. Touahra)

use of greenhouse gas (CO₂ and CH₄) and/or by reducing energy consumption. Catalytic dry reforming of methane (DRM) (also known as CO₂ reforming of methane) converts both CO₂ and CH₄ to syngas (CH₄ + CO₂ ↔ 2CO + 2H₂); the reaction has been proposed by many researchers as one of the possible solutions targeted at reducing the amount of CO₂ and CH₄ in our environment. The resulting intermediate is widely applied in the Fischer–Tropsch synthesis [1,2], to make other value-added hydrocarbons. However, the dry reforming of methane requires a high temperature (typically above 640 °C) [3]. DRM has been widely investigated over Ni-based catalysts; rapid deactivation of the utilized catalysts is primarily due to carbon formation and sintering of the active phase. Carbon deposition on the surface of catalysts mainly occurs from the following side reactions (Equations (1), (2), (3) and (4)). The reverse water–gas shift reaction can also occur as a side-reaction in which some of the H₂ from the CH₄ decomposition reacts with the CO₂ to produce H₂O and CO (Equation (5)) [4-9].



In this regard, many efforts were devoted to improving the activity and coke-resistance of nickel-based catalysts. Among the various strategies proposed is the incorporation of other metal promoters such as Mn, Zr, La, Zn, Fe, Mg, Ce and Cu [10-14], alongside increasing the catalysts' surface basicity [15,16], and additional control of the active element particle size [17,18]. The addition of metal promoters had also attracted much attention from the scientific community [19]. More recently, the effect of Mn promoter in Ni-based catalysts used for DRM reactions were investigated by many researchers [20-24]. Yao *et al.* [24] studied the effect of Zr and Mn promotion in Ni/SiO₂ catalysts. The authors found that the addition of Mn lead to the formation of smaller particle size of Ni, which enhanced the interaction with the support. Thus, Ni-Mn/SiO₂ catalyst showed higher activity and better ability to restraining carbon deposition. The introduction of Zr increased the reducibility of Ni/SiO₂ catalyst and enhanced the initial catalytic activity, but suffered from carbon deposition had which lead to obvious deactivation.

The promotion effect of Mn on Ni-based catalysts was also studied by Mousavi *et al.* [22] The authors concluded that the incorporation of Mn into the cerium oxide 10%Ni/Ce_{1-x}Mn_xO₂ (0, 0.05, 0.25, 0.50, 0.75 and 1) increased the BET surface area and improved the catalytic activity and resistance against carbon formation. They also found that the catalytic activity decreased in the presence of excess Mn. Recently, our group studied a new catalyst system based on manganese incorporated within NiAl hydrotalcite derived structures in CO₂ reforming of methane reaction [10]. NiAl and MnAl hydrotalcites were synthesized following co-precipitation method and NiAl-MnY (Y = ethylenediaminetetraacetic acid (EDTA)) catalyst was synthesized *via* intercalation of MnY²⁻ in the interlayer space of NiAl hydrotalcite type structure following an ionic exchange protocol. It was found that during DRM reaction, NiAl-MnY catalyst achieved the best result compared to NiAl catalyst in terms of minimizing carbon deposition and enhancing gas conversions at 700 °C. The elimination of carbon from the surface of the catalysts was explained by the possibility of *in-situ* redox looping mechanism in the form of Mn₃O₄/C/MnO/CO₂ [10].

The present paper aims at studying the effect of Mn_xO_y positioning within the structure of Ni/Al₂O₃ hydrotalcite-derived catalysts systems to generate newly derived catalysts for application in DRM reaction. For comparison, we apply the co-precipitation method to synthesize Ni/Al₂O₃, Ni/Mn_xO_y-Al₂O₃ and Ni/Al₂O₃-Mn_xO_yY hydrotalcite-derived catalysts, where Mn²⁺ is incorporated in the brucite-like layer of Ni/Al₂O₃ catalyst to form Ni/Mn_xO_y-Al₂O₃ catalyst while in the case of Ni/Al₂O₃-Mn_xO_yY, MnY²⁻ complex is intercalated in the interlayer space of Ni/Al₂O₃ hydrotalcite-derived catalysts.

2. Materials and Method

2.1. Catalysts Preparation

Ni/Al₂O₃, Ni/Mn_xO_y-Al₂O₃ and Ni/Al₂O₃-Mn_xO_yY hydrotalcite-derived catalysts were prepared *via* co-precipitation method following procedure previously described [10]. Ni/Al₂O₃ catalyst was synthesized with molar ratio (nNi²⁺/nAl³⁺) = 2, in order to induce the formation of hydrotalcite structures. The aqueous solutions of nitrate metals were added dropwise to a vigorously stirring solution of NaOH (2 M) at room temperature while pH was maintained at 12. The obtained slurry was heated at

80 °C, kept under stirring for 15 hours for maturation, and then filtered, washed with water and finally dried at 100 °C in oven overnight. In order to study the effect of Mn positioning within the Ni/Al₂O₃ hydrotalcite-derived catalysts structure (*i.e.*, in the brucite layer or in the interlayer space of hydrotalcite), we embarked on the synthesis of Ni/Mn_xO_y-Al₂O₃ sample using the co-precipitation method reported above with molar ratio (nNi²⁺/nAl³⁺) = 2.4.

The synthesis of Ni/Al₂O₃-Mn_xO_yY hydrotalcite-derived catalysts layered double hydroxide (LDH) included two steps. Firstly, an aqueous solution of MnY²⁻ complex was prepared at room temperature following a procedure previously described [10]. Mn²⁺ nitrate solution (20 mmol) was added dropwise to tetrasodium salt of (EDTA=Y) dissolved in 50 mL of water. NaOH solution (1 M) was added up to pH = 8. After stirring for 2 h, the resulting solution was filtered to remove excess (NaNO₃) solids. The second step of synthesis included dropwise addition of aqueous solution of Ni²⁺ and Al³⁺ nitrates to a solution of MnY²⁻. PH was adjusted to 12 by addition of aqueous solution of NaOH (2 M). The obtained slurry was stirred at 80 °C for 15 h under Nitrogen. The resulting MnY²⁻ intercalated in-between brucite layers of Ni/Al₂O₃ hydrotalcite-derived was filtered, washed with ultra-pure water and finally dried at 100 °C in oven overnight. Finally, the furnished materials, was subjected to calcination at 800 °C (increments of 5 °C/min) for 6 h, to afford the desired hydrotalcite-derived material.

2.2 Catalysts Characterization

Thermogravimetric analysis (TGA) was performed using Thermal Analyzer Setaram Set Sys 16/18 from room temperature to 900 °C with a heating rate of 10 °C/min in the presence of air. The chemical composition was established using inductively coupled plasma atomic emission spectroscopy (ICP-AES) in the presence of a multichannel Thermo Jarrel Ash ICAP 957 spectrometer. X-ray diffraction patterns of powdered samples were obtained using Siemens D-5000 diffractometer with Cu-K α radiation (λ = 1.5418 Å). The average particle size (d_{hkl}), following reduction, were estimated using the Debye-Scherrer formula (Equation (6)) [25].

$$d_{hkl} = \frac{0.9\lambda}{\beta_{hkl} \cos \theta} \quad (6)$$

where λ is the radiation's wavelength, β_{hkl} is the half width of the peak, and θ is the Bragg diffraction angle. The specific surface area

measured by nitrogen adsorption at -196 °C using Micrometrics Tristar 3000 and evaluated using the BET equation. Temperature-programmed reduction (TPR) and temperature programmed oxidation analysis (TPO-O₂) profiles were determined using a TriStar3000 V6.01A apparatus equipped with a TCD detector. Prior to reduction, the sample (20 mg) was flushed with argon in a quartz reactor tube, heated at 120 °C for 2 h under argon flow with a rate of 5 °C/min and cooled afterward to room temperature. The sample was submitted to a 5% H₂/Ar up flow to 900 °C with a 10 °C/min rate. The same method was also used for TPO-O₂ of the used catalysts. An oxidizing gas stream (3% O₂/He) was employed in this analysis and other steps were similar to those mentioned for the TPR-H₂ analysis. Scanning electron microscopy (SEM) images were obtained using Jeol 320 instrument. The samples were affixed to the sampling plate with carbon black tape and coated with Pt to prevent any charging effect during analysis. Transmission Electron Microscopy (TEM) images of the catalysts before and after reaction were obtained with high resolution field emission transmission electron microscope at 100 kV using JEOL-JEM-1200EX. FTIR spectra were recorded with Alpha Bruker (single reflection diamond ATR) spectrometer in the region 400-4000 cm⁻¹. X-ray photoelectron spectroscopy (XPS) surface analysis of NiAl, NiMnAl and NiAl-MnY was performed in Escalab 200R spectrometer equipped with a hemispherical electron analyzer and an Al K α X-ray source (1486.6 eV).

2.3 Catalytic Activity

Catalytic testing experiments were carried out in a continuous flow system at atmospheric pressure using a fixed-bed tubular quartz reactor. Prior to catalytic reaction, 100 mg of each sample was reduced *in-situ* under constant hydrogen flow at 750 °C for one hour. After that, the temperature was cooled down to the initial reaction's temperature and a feed gas mixture containing CH₄:CO₂: Ar in a ratio of 20:20:60 was passed through. The total gas flow rate was set to 20 mL/min. The reaction products were analyzed using gas chromatograph (Delsi), equipped with a thermal conductivity detector (TCD). The TCD uses two-meters-long stainless-steel Carboseive column, in the presence of carrier gas argon. The chromatography (GC) operating conditions: Oven temperature = 100 °C; Injector and detector temperature = 100 °C; and Temperature for the accessory = 70 °C.

3. Results and discussion

3.1 Thermogravimetric Analysis (TG/DTG)

Both TG and DTG curves of the investigated samples are given in Figure S1 in the Supplementary Materials. In every case, three losses of mass were observed; the first weight loss is attributed to the removal of interlayer water molecules. At this stage, a higher weight loss for Ni/Mn_xO_y-Al₂O₃ and Ni/Al₂O₃-Mn_xO_yY was observed compared to that of Ni/Al₂O₃ (Table 1). The cause of this is the increase in the number of interlayer water molecules resulting from the addition of manganese. The second weight loss was due to the dehydroxylation of the layered structure and the removal of interlayer anions (NO₃). In the case of Ni/Al₂O₃-Mn_xO_yY sample, a large weight loss was observed, this could be due to the decomposition of EDTA. In the third step, the weight loss could be assigned to the decomposition of all residual salt within the samples (Table 1).

3.2 Catalyst Composition Using ICP

By looking at the data obtained from elemental the chemical analysis and taking into account the amount of water loss in the samples using thermogravimetric analysis, we generate the formulae summarized in Table 2.

The experimental values of the molar ratios nNi²⁺/nAl³⁺ of the synthesized samples are very close to the theoretical values nNi²⁺/nAl³⁺ = 2, with the exception of the solid Ni/Mn_xO_y-Al₂O₃ which showed a molar ratio (nNi²⁺ + nMn²⁺)/nAl³⁺ = 2.84 instead of 2.40. This difference could be attributed to the partial incorporation of aluminum cations inside the brucite layer.

3.3 Measurement of Specific Surface Areas

The specific surface areas for all samples are shown in Table 3. The surface areas of the hydrotalcite intermediate prior to calcination showed relatively high *S*_{BET} values, except for Ni/Al₂O₃-Mn_xO_yY sample (13 m²/g). This result can be explained by the penetration of EDTA species into the pores of the materials. However, following calcination of all samples, a change in *S*_{BET} was observed. The increase in *S*_{BET} in the case of Ni/Al₂O₃ and Ni/Mn_xO_y-Al₂O₃ samples can be explained by the removal of water from the interlayer space of the hydrotalcite structures [26]. On the other hand, the large increase in *S*_{BET} in the case of Ni/Al₂O₃-Mn_xO_yY sample was mainly attributed to the elimination of inter-lamellar water and the pyrolysis of Y⁴⁻ ligand after heat treatment [10,27].

Table 1. TG results of precursors solids.

Samples	First weight loss (%)	Temperature (°C)	Second weight loss (%)	Temperature (°C)	Third weight loss (%)	Temperature (°C)
Ni/Al ₂ O ₃	5	83	5	221	11	330
Ni/Mn _x O _y -Al ₂ O ₃	8	227	5	327	9	405
Ni/Al ₂ O ₃ -Mn _x O _y Y	12	225	24	303	8	580

Table 2. Chemicals composition and proposed formula for the prepared samples.

Samples	Chemical composition (wt %)					Proposed formula	Experimental molar ratio (M ²⁺ /Al ³⁺)	Theoretical molar ratio (M ²⁺ /Al ³⁺)
	Mn	Ni	Al	N	C			
Ni/Al ₂ O ₃	-	39.32	8.90	4.81	0.45	[Ni _{0.67} Al _{0.33} (OH) ₂] [(NO ₃) _{0.34} (CO ₃) _{0.037} ; 0.30 H ₂ O]	2.03	2
Ni/Mn _x O _y -Al ₂ O ₃	6.40	37.45	7.21	4.64	0.51	[Mn _{0.11} Ni _{0.63} Al _{0.26} (OH) ₂] [(NO ₃) _{0.33} (CO ₃) _{0.042} ; 0.52 H ₂ O]	2.84	2.40
Ni/Al ₂ O ₃ -Mn _x O _y Y	6.55	39.02	9.24	0.16	10.85	[Ni _{0.66} Al _{0.34} (OH) ₂] [(NO ₃) _{0.011} (MnY) _{0.119} ; 0.93 H ₂ O]	1.94	2

Table 3. Textural proprieties and crystallographic parameters of the obtained solids.

Samples	BET Surfaces area (m ² /g)				The lattice parameters				Crystallite size (nm)					
	Precursors	Calcined	Reduced	Used	d ₍₁₁₀₎	a (Å)	d ₍₀₀₃₎	c(Å)	Reduced			Used		
									^a Ni ⁰	^b Ni ⁰	^c Ni ⁰	^a Ni ⁰	^b Ni ⁰	^c Ni ⁰
Ni/Al ₂ O ₃	79	105	98	75	1.514	3.028	8.946	26.838	19	20	18	27	29	30
Ni/Mn _x O _y -Al ₂ O ₃	90	121	114	101	1.607	3.219	8.897	26.691	7.5	8	7.5	13.5	14	14.5
Ni/Al ₂ O ₃ -Mn _x O _y Y	13	126	124	123	1.514	3.028	14.496	43.494	7.2	7.1	7	8.3	8.8	8.5

^aNi⁰ : Calculated from XRD.
^bNi⁰ : Calculated from SEM.
^cNi⁰ : Calculated from TEM.

3.4 X-ray Diffraction Analysis

Figure 1A shows the X-ray diffractograms of the un-calcined samples. The corresponding X-ray diffractograms for Ni/Al₂O₃, and Ni/Mn_xO_y-Al₂O₃ are consistent with those expected for hydrotalcite-like structures with sharp and symmetric reflections for (003), (006), (110) and (113) planes and broad asymmetric reflexions for (012), (015) and (018) [JCPDS file 15-0087]. The position of the first two diffraction peaks (003) and (006), are related to the spacing between the sheets "c" (with $c = 3 \times d_{003} = 6 \times d_{006}$) [18]. This parameter represents the distance between two adjacent sheets. The insertion of MnY²⁻ complex causes a separation of the sheets of the LDH, which is manifested by the appearance of two additional peaks located at $2\theta = 6$ and 18° .

It can be readily seen that the diffractogram of Ni/Al₂O₃-Mn_xO_yY has a specific set of reflection peaks that significantly differ from the counterpart materials. Indeed, the intercala-

tion of MnY²⁻ in Ni/Al₂O₃ sample which lead to the obtention of Ni/Al₂O₃-Mn_xO_yY prompted an important shift towards lower 2θ for reflection plane (003), indicating a significant increase in the interlayer separation from 8.946 to 14.496 Å (Figure 1A). The results of XRD experiments for the calcined samples (at 800 °C) are presented in Figure 1B. Following thermal treatment, the hydrotalcite structure of the samples were destroyed. XRD patterns of Ni/Al₂O₃ sample showed the formation of NiO species [JCPDS file 47-1049] and NiAl₂O₄ spinel [JCPDS file 10-0339]; an amorphous aluminum oxide phase (Al₂O₃) should also be formed (not detected in XRD) [28]. The Mn-containing samples exhibited peaks corresponding to NiO, NiAl₂O₄ and Mn₃O₄ [JCPDS file 24-0734].

3.5 FTIR Analysis

FTIR spectroscopy can provide valuable information on the identification of the anion bonds in the inter lamellar space. FTIR spectra

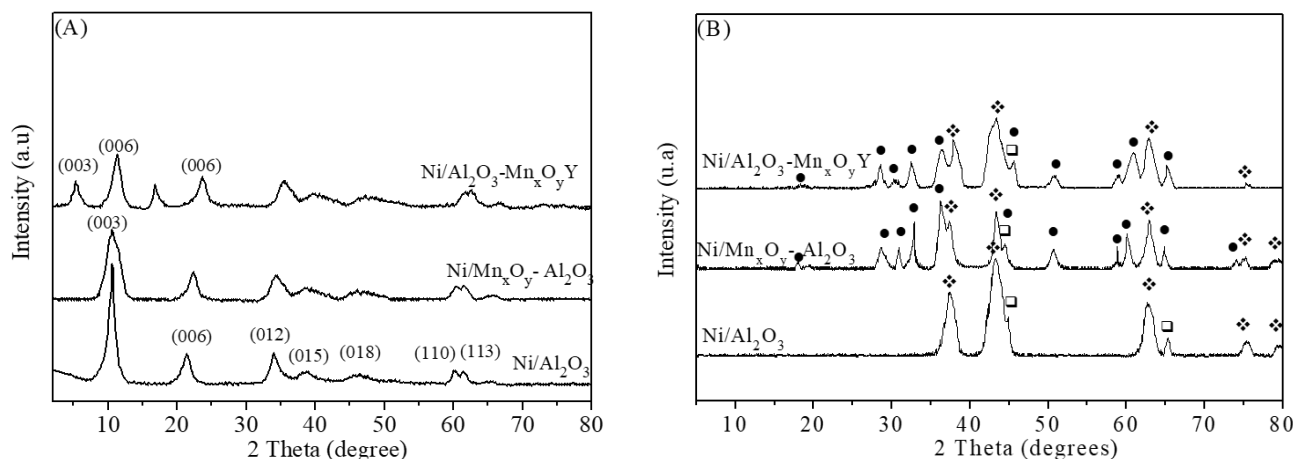


Figure 1. XRD of: (A) precursors samples and (B) their calcined products. ●Mn₃O₄, ♦NiO and □NiAl₂O₄.

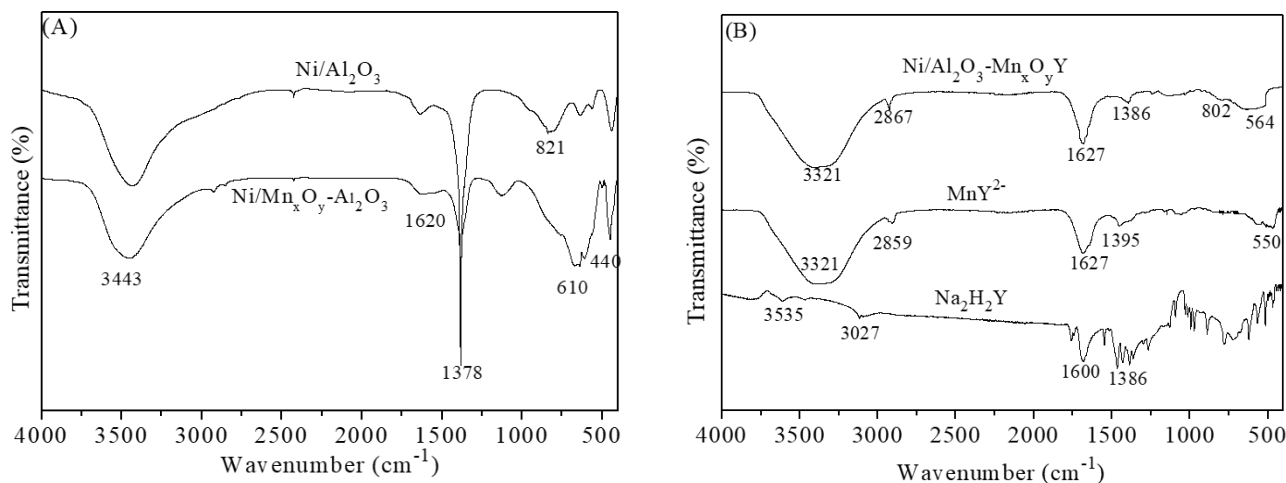


Figure 2. FTIR of: (A) Ni/Al₂O₃, Ni/Mn_xO_y-Al₂O₃ and (B) Na₂H₂Y, MnY²⁻ and Ni/Al₂O₃-Mn_xO_yY.

of Ni/Al₂O₃ and Ni/Mn_xO_y-Al₂O₃ samples are shown in Figure 2A, while that of Ni/Al₂O₃-Mn_xO_yY solid is shown in Figure 2B. The bands present are almost similar; the characteristic vibrational bands of the existing groups within the LDH structure are similar to those previously listed in literature [12,26]. In addition, we also note those bands forming part of the EDTA structure inserted into the inter lamellar space of Ni/Al₂O₃-Mn_xO_yY. The very strong peak at 1378 cm⁻¹ can be assigned to the stretching vibration of NO₃⁻ group. The apparent band at 3443 cm⁻¹ is attributed to the O-H stretching vibration of physically adsorbed water. The band around 1620 cm⁻¹ is attributed to the deformation vibrations of water δ(H₂O). The FTIR spectra also confirmed the successful intercalation of MnY²⁻ in-between the layers of the brucite. Two strong bands located at 1627 cm⁻¹ and 1386 cm⁻¹ are attributed to the asymmetric and symmetric vibrations of carboxylate group (-COO⁻) in EDTA [10,27,29]. In the low frequency region (1000 and 400 cm⁻¹), the adsorption peaks correspond to the lattice vibration modes (Al-O, Ni-O and Mn-O).

3.6 Temperature Programmed Reduction (H₂-TPR)

H₂-TPR profiles for all samples are plotted in Figure 3. H₂-TPR of Ni/Al₂O₃ sample showed a profile with a main peak at 530 °C, which corresponds to the reduction of free NiO. A broad peak was observed at around 677 °C, this reduction peak corresponds to the reduction of nickel species in NiAl₂O₄ phase, which was previously observed during XRD analysis.

H₂-TPR of Ni/Mn_xO_y-Al₂O₃ and Ni/Al₂O₃-Mn_xO_yY showed three reduction peaks. The

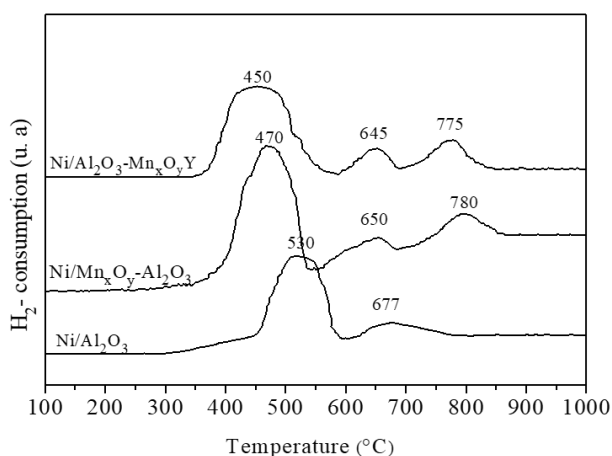


Figure 3. TPR profiles of Ni/Al₂O₃, Ni/Mn_xO_y-Al₂O₃ and Ni/Al₂O₃-Mn_xO_yY.

first peak was observed at 450 °C and 470 °C for Ni/Al₂O₃-Mn_xO_yY and Ni/Mn_xO_y-Al₂O₃ respectively, corresponding to the reduction of free NiO on the surface of the catalyst, the second peak was observed around 650 °C which can be attributed to reduction of nickel strongly bound to Al₂O₃ phase. The last peak centered at 780 °C could be assigned to the reduction of Ni²⁺ and/or Mn_xO_y further situated inside the amorphous structure of Al₂O₃ phase. Although H₂ reduction of Mn_xO_y species was found to generally occur at lower temperature range, [24, 30] previous findings by our group had shown elevated reduction temperatures for Mn_xO_y in materials derived from MnAl hydrotalcite systems (H₂-TPR not shown here) [10]. Based on previous studies [10], and in agreement with results from other literature material [31], we can conclude that the presence of Mn in Al solids favored a displacement of the reduction peak of Ni towards lower temperatures, this could be explained by the presence of strong interactions between Mn and Al₂O₃, which consequently weakens the interaction between Ni and Al₂O₃. H₂-TPR also helps us assessing the amount of reducible species of a material. The hydrogen consumptions, expressed in mmol/g of catalyst, are summarized in Table 4. In all catalysts, the H₂ consumption between 300 and 600 °C roughly corresponds to that expected for the complete reduction of the NiO phase to metallic Ni⁰. In the second H₂ consumption (600-750 °C), the amount of hydrogen is equal to that needed for reducing nickel in NiAl₂O₄ phase to Ni⁰. However, H₂ consumption between 750 and 850 °C was observed in the case of Ni/Al₂O₃-Mn_xO_yY and Ni/Mn_xO_y-Al₂O₃ catalyst, which could correspond to the surface reduction of Mn₃O₄ to

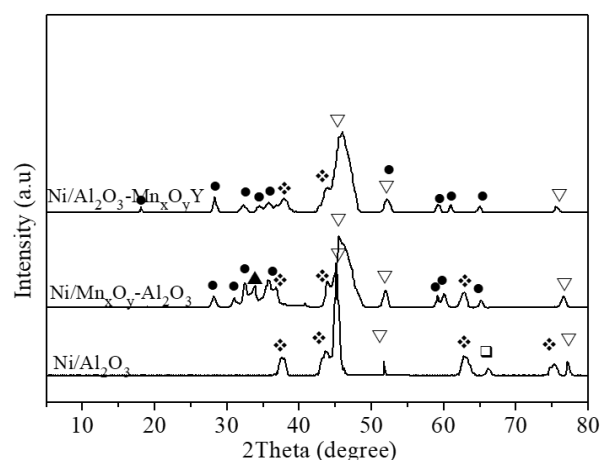


Figure 4. XRD of reduced catalysts at 750 °C. ●Mn₃O₄, ◆NiO, ▼Ni⁰, ▲MnO and □NiAl₂O₄.

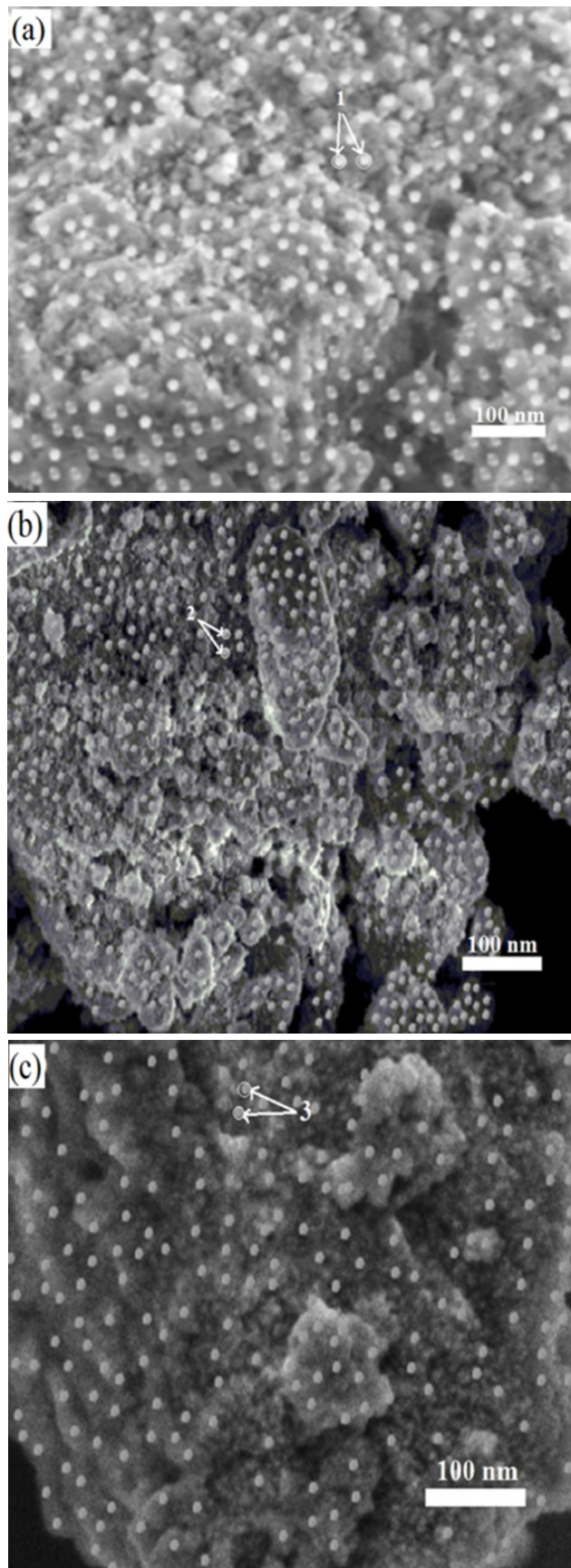


Figure 5. SEM for the reduced samples (a) Ni/Al₂O₃, (b) Ni/Mn_xO_y-Al₂O₃ and (c) Ni/Al₂O₃-Mn_xO_yY.

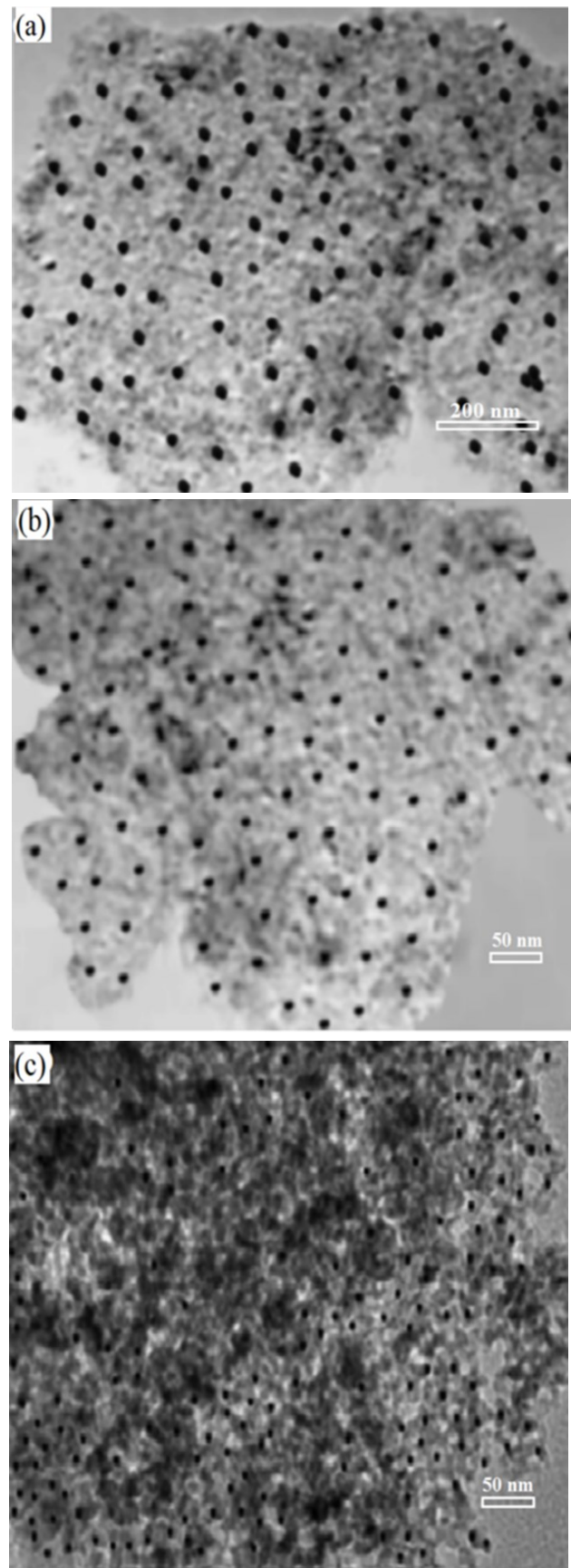


Figure 6. TEM for the reduced samples (a) Ni/Al₂O₃, (b) Ni/Mn_xO_y-Al₂O₃ and (c) Ni/Al₂O₃-Mn_xO_yY.

MnO, as shown in the XRD results after reduction (Figure 4).

3.7 Characterization of Catalysts after Reduction

Catalysts were reduced with flowing hydrogen (T reduction = 750 °C, flow (H₂) = 20 mL/min, for 1 hour). The obtained samples were analyzed using different techniques, *i.e.*, XRD, BET, SEM-EDX, TEM and XPS.

3.7.1 X-ray diffraction after reduction

For all samples, XRD patterns (Figure 4) obtained after reduction showed the presence of Ni⁰ [JCPDS file 04-0850], identified by the diffraction lines located at 2θ = 44.50°, 51.84° and 76.01°. In addition, XRD profile of the catalyst after reduction demonstrated the partial presence of NiO. Mn₃O₄ were also observed in the case of Mn-containing samples. XRD pattern of Ni/Mn_xO_y-Al₂O₃ also shows a small peak at 2θ = 33.7° which corresponds to the presence of MnO. Interestingly, the Ni particle size in Ni/Al₂O₃ (19 nm) was found to be greater than that of Ni/Mn_xO_y-Al₂O₃ (7.5 nm) and Ni/Al₂O₃-Mn_xO_yY (7.2 nm) catalysts (Table 3).

3.7.2 BET surface of reduced samples

Evaluation of the specific surface area of all catalysts after reduction was also studied. Indeed, data shown in Table 3 demonstrated that the reduction step lead to a small decrease in the specific surfaces areas in the case of Ni/Al₂O₃ and Ni/Mn_xO_y-Al₂O₃ catalysts. On the other hand, in the case of Ni/Al₂O₃-Mn_xO_yY, the specific surface area remained constant after reduction (126-124 m²/g). Albeit the decrease in surface areas in Ni/Al₂O₃ and Ni/Mn_xO_y-Al₂O₃ compounds was in accordance with the general sintering of nanoparticles forming part of the catalysts, we clearly notice a different trend with regards to the larger surface area observed in Ni/Al₂O₃-Mn_xO_yY, which indicates a much more stable surface morphology that prompted resistance in surface particle agglom-

eration. These results can be explained by the introduction of Mn shall minimize Ni particle agglomeration via the prevention of van der Waals forces between Ni particles. Therefore, small crystallite size of Ni particles is formed, thus, leading to the obtention of high dispersion in Ni/Al₂O₃-Mn_xO_yY.

3.7.3 SEM and TEM analyses after reduction

The morphology of Ni/Al₂O₃, Ni/Mn_xO_y-Al₂O₃ and Ni/Al₂O₃-Mn_xO_yY after reduction was analyzed by SEM-EDX and TEM (Figure 5, S2 and Figure 6, respectively).

Following reduction, all catalysts demonstrated the presence of smaller and evenly distributed Ni particles on the surface of the catalysts.

The average particle size of Ni⁰ in the reduced samples, calculated from the SEM and TEM images, are in good agreement with the average size calculated by the XRD method (Table 3). It is interesting to point out that the size of Ni⁰ nickel particles are smaller in the case of Mn-containing catalysts, which can suggest that the addition of Mn in the solid matrix has a considerable effect in decreasing the particles sizes.

3.7.4 XPS after reduction

XPS spectra of Ni/Al₂O₃, Ni/Mn_xO_y-Al₂O₃ and Ni/Al₂O₃-Mn_xO_yY catalysts after reduction are displayed in Figure 7. Figure 7A shows the Ni 2p_{3/2} XPS spectrum of three catalysts after reduction at 750 °C (before reaction). The figure shows two peaks having binding energies of 852.4 and 856.3 eV for all catalysts, which are assigned, respectively, to metallic Ni and NiO, these results are in agreement with previously reported data in the literature [32,33]. The presence of NiO on the surface of the reduce catalysts (prior reaction) might have been owing to the re-oxidation of Ni⁰ when the reduced samples were exposed to air. Figure 7B shows the XPS spectra of Mn 2p on Ni/Mn_xO_y-Al₂O₃ and Ni/Al₂O₃-Mn_xO_yY catalysts. The

Table 4. Surface element compositions.

Catalysts	^a H ₁	^b H ₂	^c H ₂	^d O _{Lattice}	^d O _{Adsorbed}	O _{Adsorbed} /O _{Lattice}	^e Mn ²⁺ (% atom)	
	(mmol.gcat ⁻¹)	(mmol.gcat ⁻¹)	(mmol.gcat ⁻¹)	(%)	(%)		Before reaction	
Ni/Al ₂ O ₃	7.721	2.801	-	65.4	34.6	0.52	-	-
Ni/Mn _x O _y -Al ₂ O ₃	7.911	3.212	2.792	58.9	41.1	0.70	67.4	32.6
Ni/Al ₂ O ₃ -Mn _x O _y Y	6.912	2.912	2.915	56.8	43.2	0.76	63.3	36.7

^aThe hydrogen consumption at T1=400-600 °C, calculated from TPR-H₂.

^bThe hydrogen consumption at T2=600-750 °C, calculated from TPR-H₂.

^cThe hydrogen consumption at T3=750-850 °C, calculated from TPR-H₂.

^dFrom O1s of XPS analysis.

^eFrom Mn 2p of XPS analysis before reaction.

binding energy of Mn 2p_{3/2} at 641.5 eV revealed the presence of Mn species (either in the form of Mn³⁺ or Mn²⁺) on the surface of Ni/Mn_xO_y-Al₂O₃ and Ni/Al₂O₃-Mn_xO_yY catalysts prior to CO₂ reforming of methane reaction, since the differences between the binding energy values of Mn³⁺ and Mn²⁺ were small [34,35]. In addition, all three samples showed Al 2p peak (Figure 7C) located at a binding energy of 75.5 eV, which can be ascribed to Al³⁺ ions [36,37]. In all samples, the positions of this peak did not change, while the intensity level was stronger in Ni/Al₂O₃ catalyst. The corresponding XPS spectra of O 1s in all catalysts had two distinct peaks shown in Figure 7d. One located at 529.2 eV, attributed to the lattice oxygen, while the peak placed at 532.2 eV can be ascribed to oxygen species adsorbed on the surface. The ratio of O_{Adsorption}/O_{Lattice} is listed in Table 4. The decrease in O_{Adsorption}/O_{Lattice} value followed the order of Ni/Al₂O₃ < Ni/Mn_xO_y-Al₂O₃ < Ni/Al₂O₃-Mn_xO_yY, implying more surface

oxygen adsorbed on Ni/Al₂O₃-Mn_xO_yY catalyst. Interestingly, we notice the presence of more surface adsorbed oxygen on Ni/Al₂O₃-Mn_xO_yY than Ni/Mn_xO_y-Al₂O₃ which can indicate the presence of different surface morphologies and/or characteristics arising from the different methodologies used to incorporate Mn in the first place.

3.8 Catalytic Performance on CO₂ Reforming of Methane

3.8.1 Role of Mn in The Catalyst Activation of CO₂ Reforming Reaction

The catalytic performance of our synthesized catalysts were evaluated at 700 °C in the reaction of CO₂ reforming reaction following an “in situ” H₂ reduction at 750 °C for 1 h. The catalytic performance and selectivity results are presented in Figure 8. Mn-based catalysts showed higher catalytic activity than Ni/Al₂O₃. The conversion of CH₄ increased from 82%

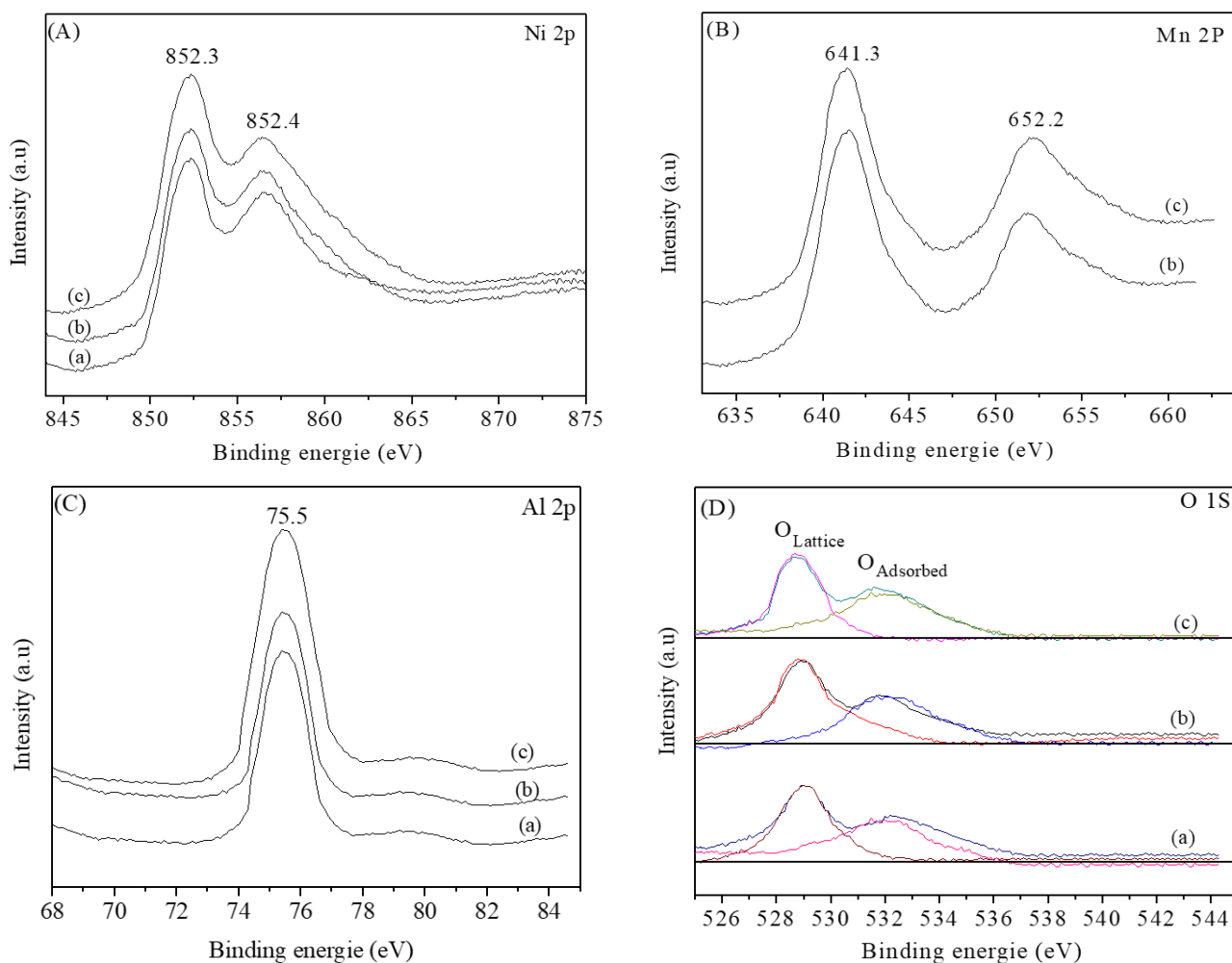


Figure 7. XPS spectra of (A): Ni 2p, (B): Mn 2p, (C): Al 2p and (D): O 1s of reduced samples (a) Ni/Al₂O₃, (b) Ni/Al₂O₃-Mn_xO_yY and (c) Ni/Mn_xO_y-Al₂O₃.

(Ni/Al₂O₃) to 86% (Ni/Mn_xO_y-Al₂O₃) and 94% (Ni/Al₂O₃-Mn_xO_yY), whereas CO₂ conversion increased from 86% (Ni/Al₂O₃) to 88% and 94% in the case of Ni/Mn_xO_y-Al₂O₃ and Ni/Al₂O₃-Mn_xO_yY, respectively. For Ni/Al₂O₃ and Ni/Mn_xO_y-Al₂O₃ catalysts, it was found that the conversion of CO₂ was higher than that of CH₄ while H₂/CO molar ratio (Figure 8C) in the resulting syngas was slightly lower than the desired stoichiometric ratio of 1 after 50 h of reaction time; this was owing to the presence of concurrent hydrogenation of carbon dioxide (CO₂ + 2H₂ → C + 2H₂O) and/or reverse water-gas shift reaction (CO₂ + H₂ → CO + H₂O).

Ni/Al₂O₃ showed relatively lower CH₄ and CO₂ conversions when compared to Ni/Mn_xO_y-Al₂O₃ and Ni/Al₂O₃-Mn_xO_yY catalysts. In addition, it is important to note that in Ni/Al₂O₃ catalyst, the activity started to decrease after 30 hours of reaction time, such phenomenon was not observed in the case of Ni/Mn_xO_y-Al₂O₃ and Ni/Al₂O₃-Mn_xO_yY according to Ray *et al.* [38] this result is due to the incorporation of

Mn in Ni-based catalyst which plays a good role in promoting a synergistic effect that further stabilizes the catalyst. The addition of Mn leads to the formation of well dispersed Ni⁰ nanoparticles on the surface of the catalyst, and thus induces large specific surface areas after reduction (Table 3). In addition, previous work by our group also elucidated the possibility of deposited carbon being oxidized in the presence of manganese oxide (Mn₃O₄) to release carbon monoxide CO: (Mn₃O₄ + C ↔ 3MnO + CO) [10]. This was confirmed by the presence of Mn₃O₄ and MnO species prior to and after reaction, respectively. This hypothesis was further exploited by Gan *et al.* [39].

Guo *et al.* [30] also showed that the addition of manganese to the Ni/Al₂O₃ catalyst treated by N₂ glow discharge plasma, improved the catalytic performance by about 10% at 700 °C for the methane dry reforming reaction. The authors found that the percentage of Mn plays a very important role in catalytic activity; but that there is an optimal manganese content as for any promoter element of the catalytic activity. They reported that the catalyst (5% Mn-Ni/Al₂O₃) gave better catalytic activity compared to other catalysts (10% Mn-Ni/Al₂O₃) and (15% Mn-Ni/Al₂O₃). Mousavi *et al.* [22] also investigated the effects of the incorporation of Mn to cerium oxide 10% Ni/Ce_{1-x}Mn_xO₂ for the methane dry reforming. The catalytic results indicated that the incorporation of Mn into the catalyst carrier slightly decreased the catalytic activity. However, the catalytic stability was improved upon the addition of Mn. 10% Ni/Ce_{0.95}Mn_{0.05}O₂ catalyst exhibited the highest activity and stability compared to nickel catalyst supported on pure ceria, this was due to the low content of manganese, interaction be-

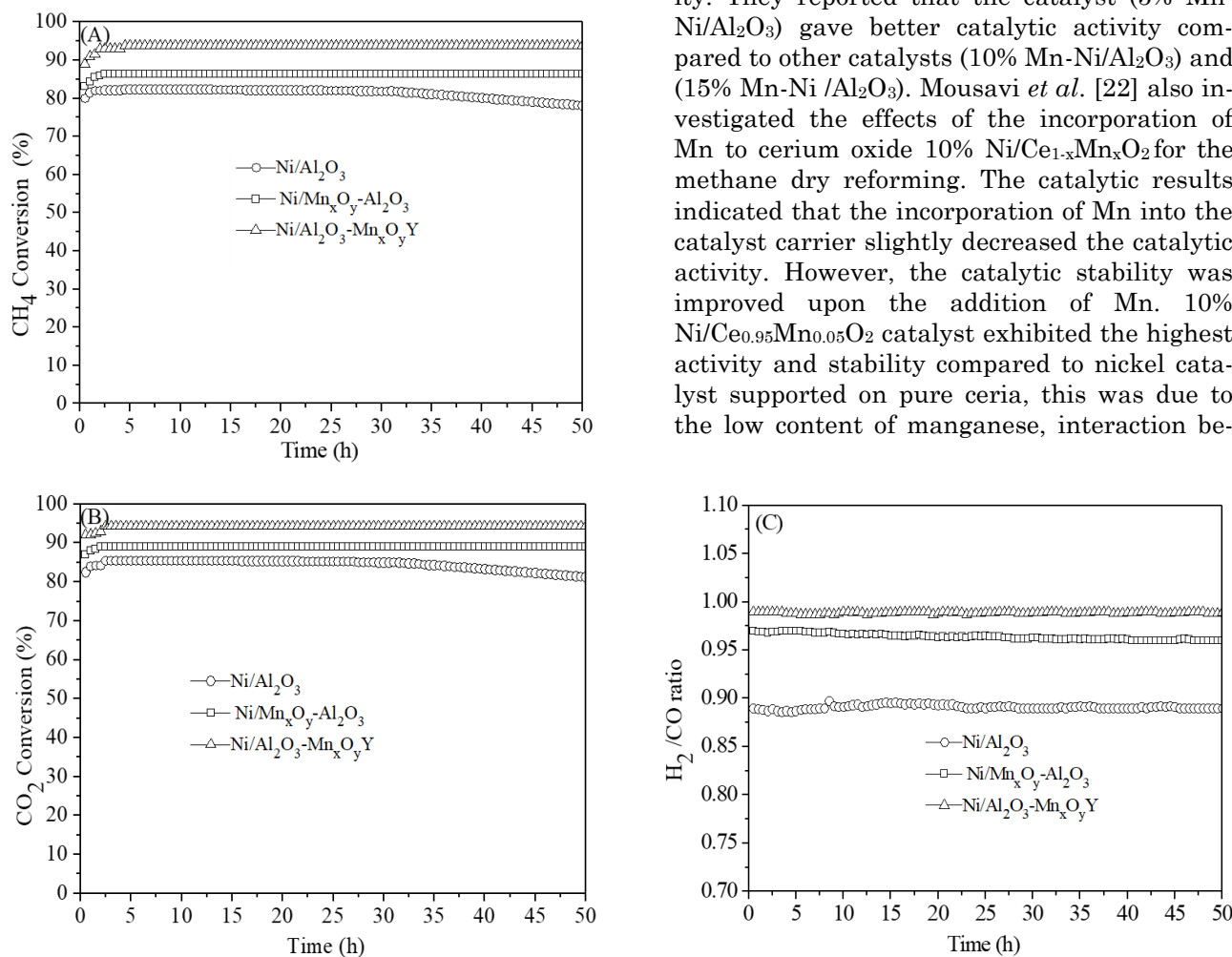


Figure 8. (A) CH₄ conversion, (B) CO₂ conversion and (C) H₂/CO ratio obtained during DRM.

tween manganese and ceria, and formation of the solid state solution, which improves the number of oxygen vacancies. The increase in oxygen vacancies was also found to improve the activity and coke resistance. Liu *et al.* [20] previously added La, Al and Mn to Fe-clay based Ni. The introduction of La, Al and Mn was found to affect the specific surface area and catalyst basicity. Also, the presence of La, Al and Mn resulted in smaller and further promoted Ni dispersion. Based on DRM results, La/Al-promoted catalysts led to improvement of the catalytic performance whereas Mn-promoted catalysts inhibited it.

3.8.2 Influence of Mn Position on Catalyst Stability and Carbon Formation

In order to gain more understanding about the high performance of Ni/Al₂O₃-Mn_xO_yY catalyst, the spent catalyst was characterized using XRD, SEM, TEM, TPO-O₂ and XPS. The surface areas of all spent catalysts are incorporated in Table 3. It is clear that following CO₂ reforming of methane reaction, we observe a decrease in the surface area. In the case of Ni/Al₂O₃ catalyst, the surface area decreased from (105-75 m²/g). Incorporation of manganese in the brucite layer also resulted in a decrease in surface area, (121-101 m²/g). The surface area of Ni/Al₂O₃-Mn_xO_yY catalyst, where manganese is located in the interlayer space, remained unchanged (126-123 m²/g), suggesting a better resistance to sintering and/or carbon deposition. These results also suggests that the positioning of Mn within the HDL structure plays an important role in the thermal stability of the solid.

Figure 9 shows XRD profiles of all spent catalysts. Phases corresponding to NiO and Ni⁰

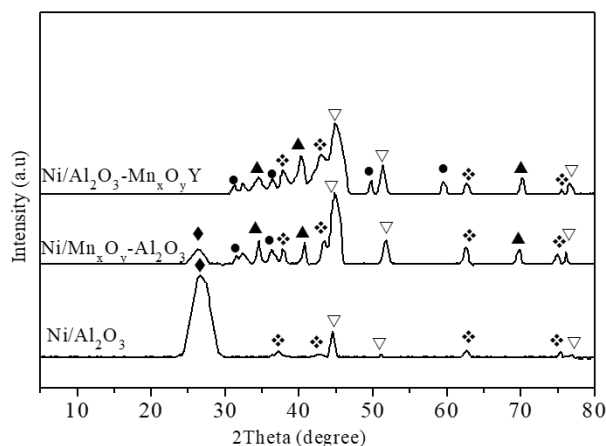


Figure 9. XRD of the used catalysts. ●Mn₃O₄, ◆NiO, ▽Ni⁰, ▲MnO and ◆carbon.

were observed at around $2\theta = 37^\circ, 44^\circ, 62^\circ, 76^\circ$ and $2\theta = 44^\circ, 51^\circ, 76^\circ$, respectively. Also, the diffractograms of the manganese-containing catalysts have shown the presence of MnO and Mn₃O₄. The presence of NiO phase suggested that the re-oxidation of a small part of Ni⁰ species following contact with air, given the fact that the analysis was carried out ex-situ. XRD analysis of Ni/Al₂O₃ and Ni/Mn_xO_y-Al₂O₃ catalysts also demonstrated the presence of carbon deposition at $2\theta = 27^\circ$ [JCPDS file 41-1487], however, this peak is much smaller in Ni/Mn_xO_y-Al₂O₃ catalyst. It is also important to note that this peak is totally absent in the diffractograms of Ni/Al₂O₃-Mn_xO_yY catalyst. Probably, this result is due to the presence of manganese which lead to the total or partial elimination of carbon according to the reaction (Mn₃O₄ + C \leftrightarrow 3MnO + CO). Manganese oxides Mn₃O₄ and MnO are clearly observed in XRD of both catalysts. Figure 9 shows further examination of these results revealed that, depending on the position of manganese in the hydrotalcite structure, surface carbon deposition is totally or partially eliminated. In our study, we found a clear distinction between catalysts derived from Mn being in the interlayer space of the Ni/Al₂O₃ hydrotalcite structure (*i.e.*, Ni/Al₂O₃-Mn_xO_yY), where the elimination of carbon was much more efficient, and when Mn is partially substituted for nickel in the hydrotalcite matrix, (*i.e.*, Ni/Mn_xO_y-Al₂O₃), where we find the presence of coke deposition but at a lower extent to that of Ni/Al₂O₃ catalyst.

SEM and TEM study of post-reaction samples are presented in Figure 10 and 11 respectively. It is clear from these images that after CO₂ reforming reaction, the carbon detected on Ni/Al₂O₃ and Ni/Mn_xO_y-Al₂O₃ catalysts is in the form of nano-fibers. However, the absence of carbon traces was clearly noted when Ni/Al₂O₃-Mn_xO_yY was used as catalyst; such result is in agreement with the obtained XRD results. In Table 3, we have incorporated the size values of Ni⁰ particles obtained from SEM, TEM and XRD for all used catalysts after 50 hours of reaction time at 700 °C; this is performed in order to examine the evolution of the size of particles on the surface of the catalyst. Ni⁰ particle size, estimated by SEM and TEM, are in agreement with those obtained by the XRD analyses.

The size of nickel particles increased after reaction for Ni/Al₂O₃ and Ni/Mn_xO_y-Al₂O₃ (from 19 nm to 27 nm for the former and from 7.5 nm to 13.5 nm for the latter). The increase in particle size is owed to the sintering phenomenon of Ni particles after reaction. However, a very

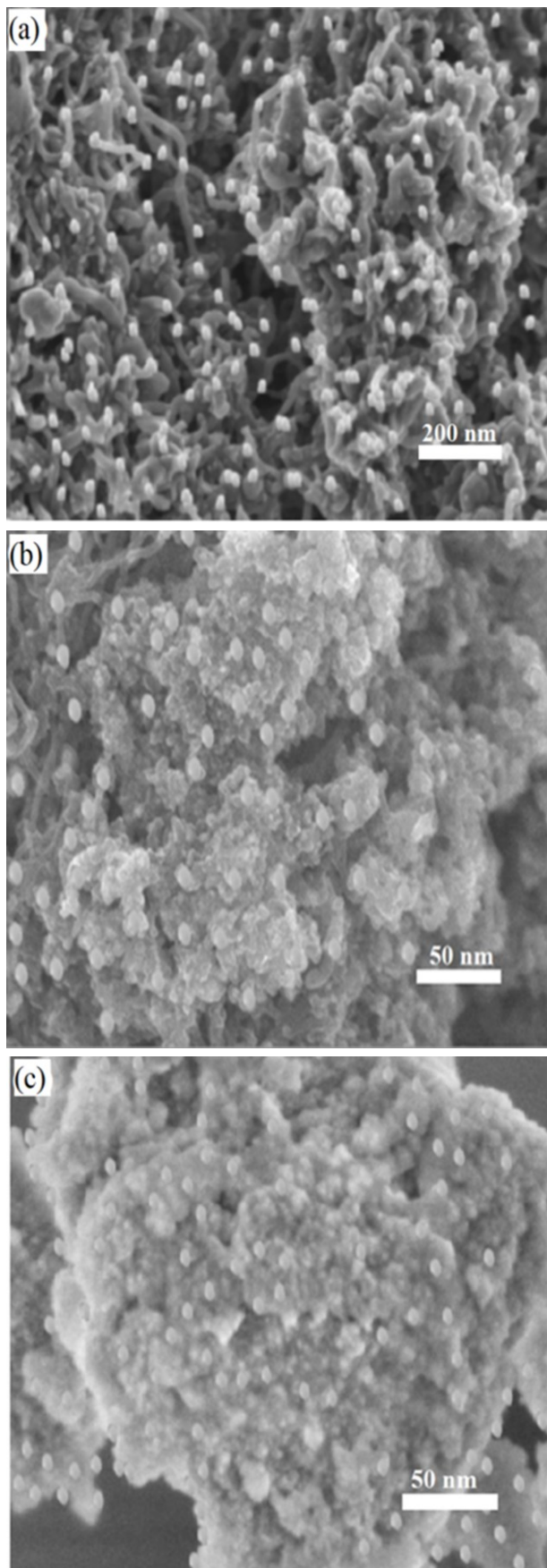


Figure 10. SEM images of: (a) Ni/Al₂O₃, (b) Ni/Mn_xO_y-Al₂O₃ and (c) Ni/Al₂O₃-Mn_xO_yY catalysts after DRM reaction.

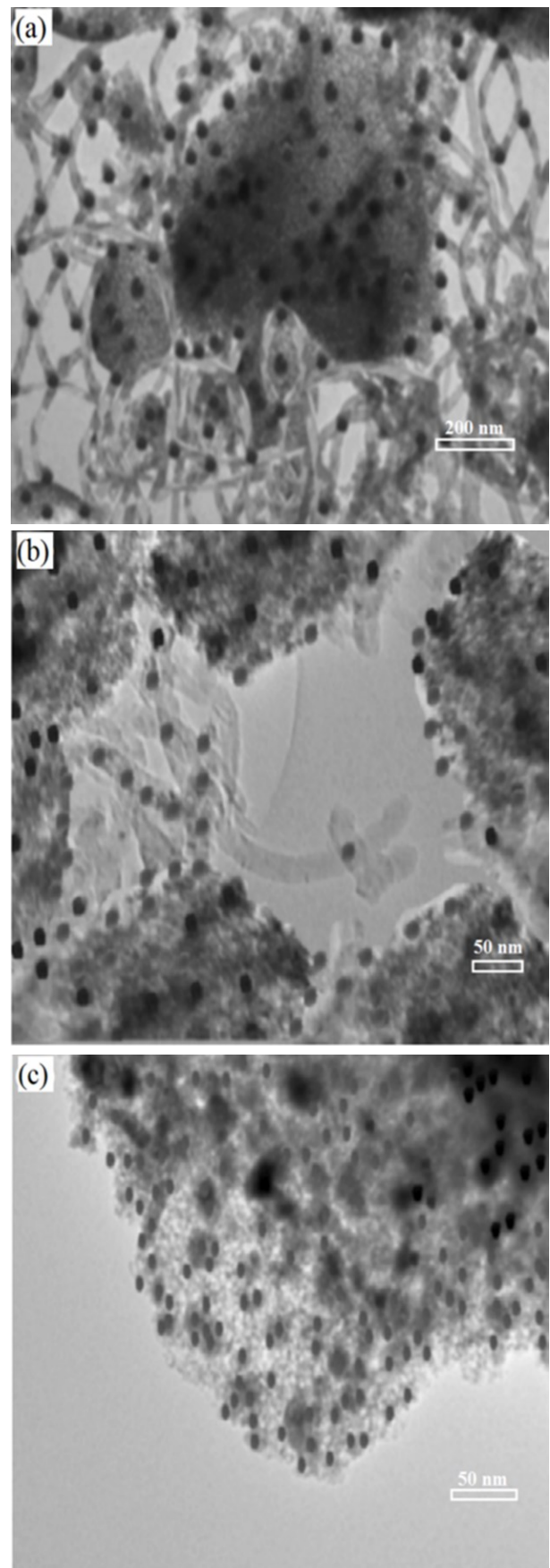


Figure 11. TEM images of (a) Ni/Al₂O₃, (b) Ni/Mn_xO_y-Al₂O₃ and (c) Ni/Al₂O₃-Mn_xO_yY catalysts, after DRM reaction.

small increase in the size of Ni⁰ is observed in the case of Ni/Al₂O₃-Mn_xO_yY catalyst (7.20 nm to 8.30 nm). These results show the beneficial effect of intercalation of Mn²⁺ cations in the inter-layer space of the catalyst; it seems that in this case, the particles would be more resistant to agglomeration during the reaction.

TPO-O₂ curves of different catalysts after reaction are shown in Figure 12. The TPO-O₂ profile of the spent catalyst shows the presence of a broad peak between 450-700 °C in the case of Ni/Mn_xO_y-Al₂O₃ catalyst. On the other hand, TPO of Ni/Al₂O₃ sample showed a broad peak with high intensity around 600 °C. The only oxidation peak appearing in the TPO-O₂ profile of the spent catalysts (Ni/Al₂O₃ and Ni/Mn_xO_y-Al₂O₃) was attributed to the oxidation of one type of carbonaceous species (filamentous carbon) on the surface of both samples [40,41]. In the case of Ni/Al₂O₃-Mn_xO_yY catalyst, no oxidation peak was detected. As can be seen, the addition of Mn within the brucite-like layer of Ni/Al₂O₃ catalyst, prompted less carbon deposition during the reaction of CO₂ reforming of methane. Therefore, we concluded that the addition of Mn in the interlayer space plays a much important role in the removal of surface carbon during the reaction of CO₂ reforming of methane.

In order to study the effect of Mn positioning within the structure of our catalysts on the carbon deposition process, the valence state of Mn on the surface of these catalysts, after being tested under DRM for 50 h, is studied using XPS. Gan *et al.* [39] previously mentioned that the split of the binding energy (ΔE) in Mn-3s spectrum is dependent on the oxidation state of Mn.

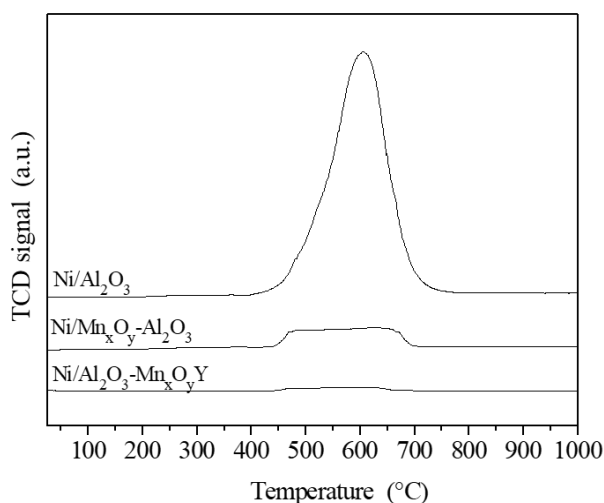


Figure 12. TPO profiles of catalysts after DRM reaction.

XPS spectra of the catalysts after reaction are displayed in Figure 13. ΔE value of Mn-containing catalysts was 6.1 eV. This result indicated the presence of Mn²⁺ species. The deposited carbon could be oxidized by Mn₃O₄ as previously mentioned ($\text{Mn}_3\text{O}_4 + \text{C} \leftrightarrow 3\text{MnO} + \text{CO}$). The improvement of catalytic performance of Ni/Al₂O₃-Mn_xO_yY catalyst is mainly attributed to the enhanced resistance to carbon deposition, as demonstrated by TEM, SEM, XRD and TPO-O₂.

In addition, the presence of Mn_xO_y in Ni/Al₂O₃ hydrotalcite derived catalyst can also enhance the basicity of the support which can lead to a better CO₂ adsorption on the surface. In our case, this clearly explains the elevated CO₂ conversion observed during the reaction of CO₂ reforming of methane. In an interesting work by Guo *et al.* [30] the authors successfully demonstrated how the addition of Mn_xO_y to Ni/Al₂O₃ catalysts, synthesized by glow discharge plasma, influenced the amount of CO₂ adsorption on the surface of their synthesized catalysts. Using CO₂-TPD measurements, the authors showed that higher Mn content (10%) prompted better CO₂ adsorption. In addition to the superior promotion of both CO₂ and CH₄ on the surface of our synthesized materials, we envisage that the presence of an *in-situ* elimination of carbon via Mn₃O₄/C/MnO/CO₂ redox looping cycle could play a synergetic role which can lead to lowering the amount of surface carbon during the reaction of CO₂ reforming of methane [40-42]. Where carbon residues are formed on the surface of reduced Ni particles, migration of carbon to neighboring Mn₃O₄ sites could be anticipated to enable the *in-situ* elimination of carbon.

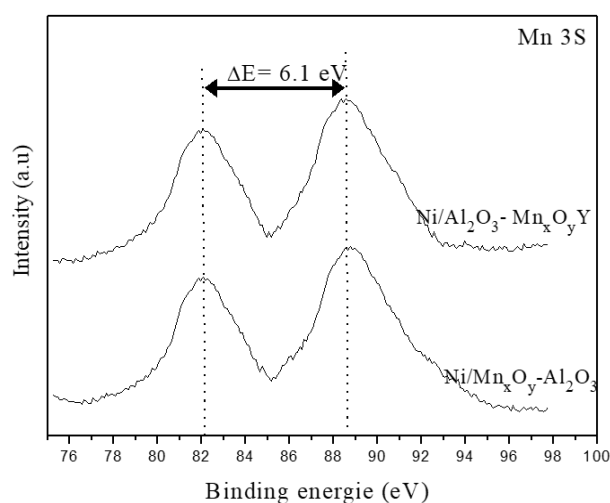


Figure 13. Mn-3s spectra of catalysts after DRM reaction.

4. Conclusion

Different types of catalysts of the type containing Ni/Al₂O₃-Mn_xO_y have been prepared by thermal decomposition of Ni/Al₂O₃, Ni/Mn_xO_y-Al₂O₃ and Ni/Al₂O₃-Mn_xO_yY (Y = EDTA) hydrotalcite precursors. The synthesized catalysts were successfully characterized using TGA, ICP, XRD, BET, FTIR, TPR-H₂, SEM-EDX, TEM, XPS, and TPO-O₂ analysis, and applied for syngas production from CO₂ reforming of methane at 700 °C. The hydrotalcite structures were confirmed using XRD analysis, while the intercalation of Mn in the interlayer space was verified using both XRD and FTIR. The XPS spectra indicated that the Mn species were reduced from 3+ to 2+ oxidation state, whereas Ni species were reduced from 2+ to 0; this was further confirmed by X-ray diffraction after reduction. The addition of Mn to Ni/Al₂O₃ increased the number of oxygen vacant sites on the support, which prompted an increase in CO₂ adsorption/conversion. The results also showed that the activity and stability of Mn-based catalysts were related to the Mn positioning; the best catalytic activity was observed with Ni/Al₂O₃-Mn_xO_yY. The characterization of Mn-based catalysts after reaction was also effected using XRD, SEM, TEM and TPO-O₂; results showed that the lack of formation of carbon deposits responsible for catalyst deactivation corroborated the stability of the reaction tests for the studied material. However, in order to gain more insight about the mechanism responsible for the low carbon formation on the surface of our Mn containing catalysts, more work using state-of-the-art on-stream techniques will need to be performed to enable better understanding of the overall situation.

Acknowledgement

The authors would like to thank Centre de Recherche Scientifique et Technique en Analyses Physico-Chimiques (CRAPC), Algeria, for the financial support.

References

- [1] Centi, G., Perathoner, S. (2009). Opportunities and prospects in the chemical recycling of carbon dioxide to fuels. *Catalysis Today*, 148, 191-205.
- [2] Al-Fatesh, A.S., Naeem, M.A., Fakeeha, A.H., Abasaheed, A.E. (2013). CO₂ Reforming of Methane to Produce Syngas over γ -Al₂O₃-Supported Ni-Sr Catalysts. *Bulletin of the Chemical Society of Japan*, 86, 742-748.
- [3] Usman, M., Daud, W.W., Abbas, H.F. (2015). Dry reforming of methane: influence of process parameters- A review *Renew. Renewable and Sustainable Energy Reviews*, 45, 710-744.
- [4] Kogler, M., Köck E.-M. Klötzer, B., Schachinger, T., Wallisch, W., Henn, R., Huck, C.W., Hejny, C., Penner, S. (2016). High-temperature carbon deposition on oxide surfaces by CO disproportionation. *Journal of Physical Chemistry C*, 120, 1795-1807.
- [5] Lavoie, J.-M. (2014). Review on dry reforming of methane, a potentially more environmentally-friendly approach to the increasing natural gas exploitation. *Frontiers in chemistry*, 2, 81-92.
- [6] Aramouni, N.A.K., Touma, J.G., Tarboush, B.A., Zeaiter, J., Ahmad, M.N. (2017). Catalyst design for dry reforming of methane: Analysis review. *Renewable and Sustainable Energy Reviews*, 82, 2570-2585.
- [7] Nezam, I., Peereboom, L., Miller, D.J. (2017). Enhanced Acrylate Production from 2-Acetoxypropanoic Acid Esters. *Organic Process Research & Development*, 21(5), 715-719.
- [8] Lødeng, R., Lunder, O., Lein, J.E., Dahl, P.I., Svenum, I.H. (2018). Synthesis of light olefins and alkanes on supported iron oxide catalysts. *Catalysis Today*, 299, 47-59.
- [9] Isobe, J., Lo, C., Childers, A., Yates, S., Winton, D. (2019). U.S. Patent No. 10,486,967. Washington, DC: U.S. Patent and Trademark Office.
- [10] Touahra, F., Sehailia, M., Halliche, D., Bachari, K., Saadi, A., Cherifi, O. (2016). (MnO/Mn₃O₄)-NiAl nanoparticles as smart carbon resistant catalysts for the production of syngas by means of CO₂ reforming of methane: Advocating the role of concurrent carbothermic redox looping in the elimination of coke. *International Journal of Hydrogen Energy*, 41, 21140-21156.
- [11] Kaydoun, M.-N., El Hassan, N., Davidson, A., Casale, S., El Zakhem, H., Massiani, P. (2015). Effect of the order of Ni and Ce addition in SBA-15 on the activity in dry reforming of methane. *Comptes Rendus Chimie*, 18, 293-301.
- [12] Dėbek, R., Galvez, M.E., Launay, F., Motak, M., Grzybek, T., DaCosta, P. (2016). Low temperature dry methane reforming over Ce, Zr and CeZr promoted Ni-Mg-Al hydrotalcite-derived catalysts. *International Journal of Hydrogen Energy*, 41, 11616-11623.
- [13] Aider, N., Touahra, F., Bali, F., Djebbari, B., Lerari, D., Bachari, K., Halliche, D. (2018). Improvement of catalytic stability and carbon resistance in the process of CO₂ reforming of methane by CoAl and CoFe hydrotalcite-

- derived catalysts. *International Journal of Hydrogen Energy*, 43, 8256-8266.
- [14] Touahra, F., Chebout, R., Lerari, D., Halliche, D., Bachari, K. (2019) Role of the nanoparticles of Cu-Co alloy derived from perovskite in dry reforming of methane. *Energy*, 171, 465-474.
- [15] Barroso-Quiroga, M.M., Castro-Luna, A.E. (2010). Catalytic activity and effect of modifiers on Ni-based catalysts for the dry reforming of methane. *International Journal of Hydrogen Energy*, 35, 6052-6056.
- [16] Wang, N., Chu, W., Zhang, T., Zhao, X. (2012). Synthesis, characterization and catalytic performances of Ce-SBA-15 supported nickel catalysts for methane dry reforming to hydrogen and syngas. *International Journal of Hydrogen Energy*, 37, 19-30.
- [17] Naeem, M.A., Al-Fatesh, A.S., Khan, W.U., Abasaheed, A.E., Fakeeha, A.H. (2013) Syngas production from dry reforming of methane over nano Ni polyol catalysts. *International Journal of Chemical Engineering and Application*, 4, 315-320.
- [18] Bhavani, A.G., Kim, W.Y., Lee, J.S. (2013). Barium substituted lanthanum manganite perovskite for CO₂ reforming of methane. *ACS Catalysis*, 3, 1537-1544.
- [19] Abdullah, B., Abd Ghani, N.A., Vo, D.-V.N. (2017). Recent advances in dry reforming of methane over Ni-based catalysts. *Journal of Cleaner Production*, 162, 170-185.
- [20] Liu, H., Hadjltaief, H.B., Benzina, M., Gálvez, M.E., Da Costa, P. (2019). Natural clay based nickel catalysts for dry reforming of methane: On the effect of support promotion (La, Al, Mn). *International Journal of Hydrogen Energy*, 44, 246-255.
- [21] Littlewood, P., Xie, X., Bernicke, M., Thomas, A., Schomäcker, R. (2015). Ni_{0.05}Mn_{0.95}O catalysts for the dry reforming of methane. *Catalysis Today*, 242, 111-118.
- [22] Mousavi, S.M., Meshkani, F., Rezaei, M. (2017). Preparation of mesoporous nanocrystalline 10% Ni/Ce_{1-x}Mn_xO₂ catalysts for dry reforming reaction. *International Journal of Hydrogen Energy*, 42, 24776-24784.
- [23] Rouibah, K., Barama, A., Benrabaa, R., Guerro-caballero, J., Tanusheree, K., Vannier, R.-N., Rubbens, A., Loberg, A. (2018). Dry reforming of methane on nickel-chrome, nickel-cobalt and nickel-manganese catalysts. *International Journal of Hydrogen Energy*, 42, 29725-29734.
- [24] Yao, L., Zhu, J., Peng, X., Tong, D., Hu, C. (2013). Comparative study on the promotion effect of Mn and Zr on the stability of Ni/SiO₂ catalyst for CO₂ reforming of methane. *International Journal of Hydrogen Energy*, 38, 7268-7279.
- [25] Melo, F., Morlanés, N. (2008). Study of the composition of ternary mixed oxides: Use of these materials on a hydrogen production process. *Catalysis Today*, 133-135, 374-382.
- [26] Holgado, M.J., Rives, V., San Román, M.S. (2001). Characterization of Ni-Mg-Al mixed oxides and their catalytic activity in oxidative dehydrogenation of n-butane and propene. *Applied Catalysis A*, 214, 219-228.
- [27] Tsyganok, A.I., Suzuki, K., Hamakawa, S., Takehira, K., Hayakawa, T. (2001) Mg-Al layered double hydroxide intercalated with [Ni(edta)]²⁻ chelate as a precursor for an efficient catalyst of methane reforming with carbon dioxide. *Catalysis letter*, 77, 75-86.
- [28] Djebarri, B., Gonzalez-Delacruz, V., Halliche, D., Bachari, K., Saadi, A., Caballero, A., Holgado, J.P., Cherifi, O. (2014). Promoting effect of Ce and Mg cations in Ni/Al catalysts prepared from hydrotalcites for the dry reforming of methane. *Reaction Kinetics, Mechanisms and Catalysis*, 111, 259-275.
- [29] Jamhour, R. (2014). Intercalation and complexation of Co (II) and Ni (II) by chelating ligands incorporated in Zn-Al layered double hydroxides. *Canadian Chemical Transactions*, 2, 306-315.
- [30] Guo, F., Xu, J.-Q., Chu, W. (2015). CO₂ reforming of methane over Mn promoted Ni/Al₂O₃ catalyst treated by N₂ glow discharge plasma. *Catalysis Today*, 256, 124-129.
- [31] Arnoldy, P., Moulijn, J.A. (1985). Temperature-programmed reduction of CoO/Al₂O₃ catalysts. *Journal of catalysis*, 93, 38-54.
- [32] Yao, L., Wang, Y., Shi, J., Xu, H., Shen, W., Hu, C. (2017). The influence of reduction temperature on the performance of ZrO_x/Ni-MnO_x/SiO₂ catalyst for low-temperature CO₂ reforming of methane. *Catalysis Today*, 281, 259-267.
- [33] Grosvenor, A.P., Biesinger, M.C., Smart, R.S.C., McIntyre, N.S. (2006) New interpretations of XPS spectra of nickel metal and oxides. *Surface Science*, 600, 1771-1779.
- [34] Wang, Y., Deng, W., Wang, Y., Guo, L., Ishihara, T. (2018). A comparative study of the catalytic oxidation of chlorobenzene and toluene over Ce-Mn oxides. *Molecular Catalysis*, 459, 61-70.
- [35] He, H., Lin, X., Li, S., Wu, Z., Gao, J., Wu, J., Wen, W., Ye, D., Fu, M. (2018) The key surface species and oxygen vacancies in MnO_x(0.4)-CeO₂ toward repeated soot oxidation. *Applied Catalysis B*, 223, 134-142.

- [36] Zhu, Z., Zhao, Q., Li, X., Li, H., Tade, M., Liu, S. (2013). Photocatalytic performances and activities in Ag-doped ZnAl₂O₄ nanorods studied by FTIR spectroscopy. *Catalysis Science and Technology*, 3, 788-796.
- [37] Jo, S.W., Im, Y., Do, J.Y., Park, N.-K., Lee, T.J., Lee, S.T., Cha, M.S., Jeon, M.-K., Kang, M. (2017). Synergies between Ni, Co, and Mn ions in trimetallic Ni_{1-x}Co_xMnO₄ catalysts for effective hydrogen production from propane steam reforming. *Renewable Energy*, 113, 248-256.
- [38] Ray, D., Reddy, P.M.K., Subrahmanyam, C. (2018). Ni-Mn/ γ -Al₂O₃ assisted plasma dry reforming of methane. *Catalysis Today*, 309, 212-218.
- [39] Gan, T., Ding, G., Chen, B., Zhi, X., Li, P., Yao, X., Hou, N., Fan, L., Zhao, Y., Li, Y. (2019). Effects of manganese oxides on the activity and stability of Ni-Ce_{0.8}Sm_{0.2}O_{1.9} anode for solid oxide fuel cells with methanol as the fuel. *Catalysis Today*, 330, 222-227.
- [40] Istadi, I., Anggoro, D.D., Amin, N.A.S., Ling, D.H.W. (2011). Catalyst deactivation simulation through carbon deposition in carbon dioxide reforming over Ni/CaO-Al₂O₃ catalyst. *Bulletin of Chemical Reaction Engineering & Catalysis*, 6(2), 129-136.
- [41] Rezaei, M. (2016). Effect of K₂O on the catalytic performance of Ni catalysts supported on nanocrystalline Al₂O₃ in CO₂ reforming of methane. *Iranian Journal of Hydrogen & Fuel Cell*, 2, 215-226.
- [42] Ramezani, Y., Meshkani, F., Rezaei, M. (2018). Preparation and evaluation of mesoporous nickel and manganese bimetallic nanocatalysts in methane dry reforming process for syngas production. *Journal of Chemical Sciences*, 130, 11-21.

Appendices: Supplementary materials

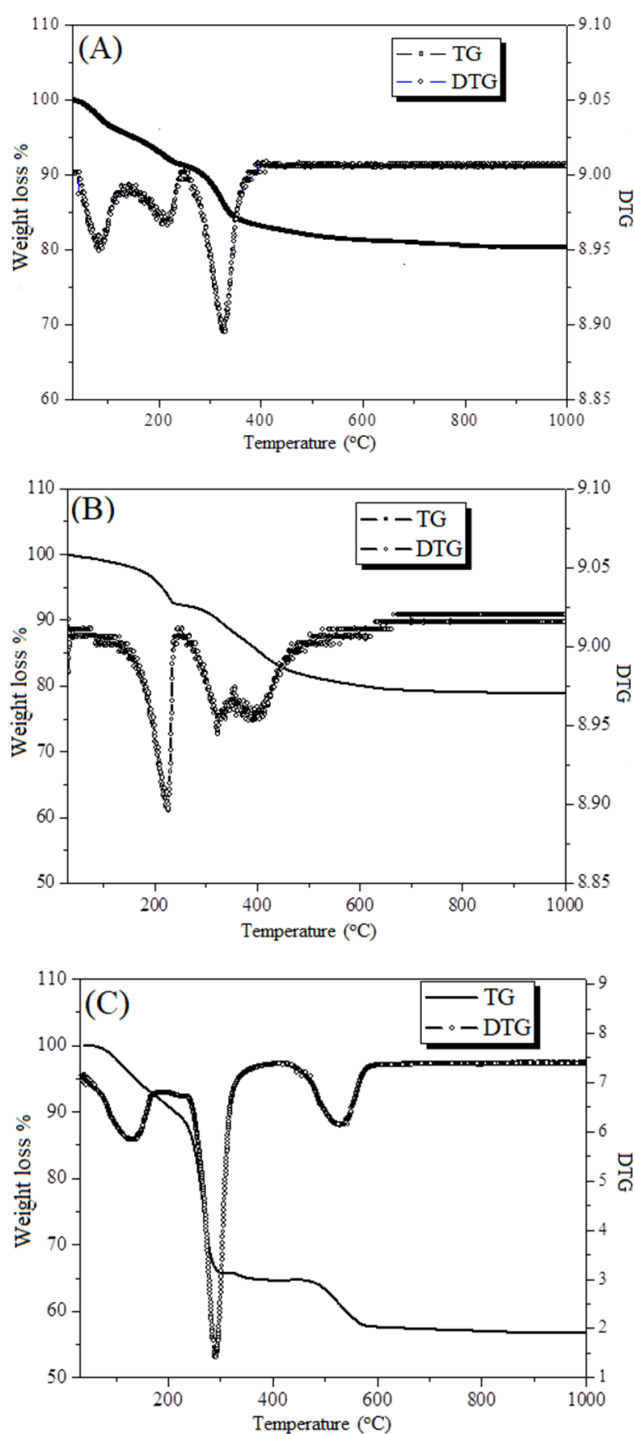


Figure S1. TG Analysis of Samples (A) Ni/Al₂O₃, (B) Ni/Mn_xO_y-Al₂O₃ and (C) Ni/Al₂O₃-Mn_xO_yY.

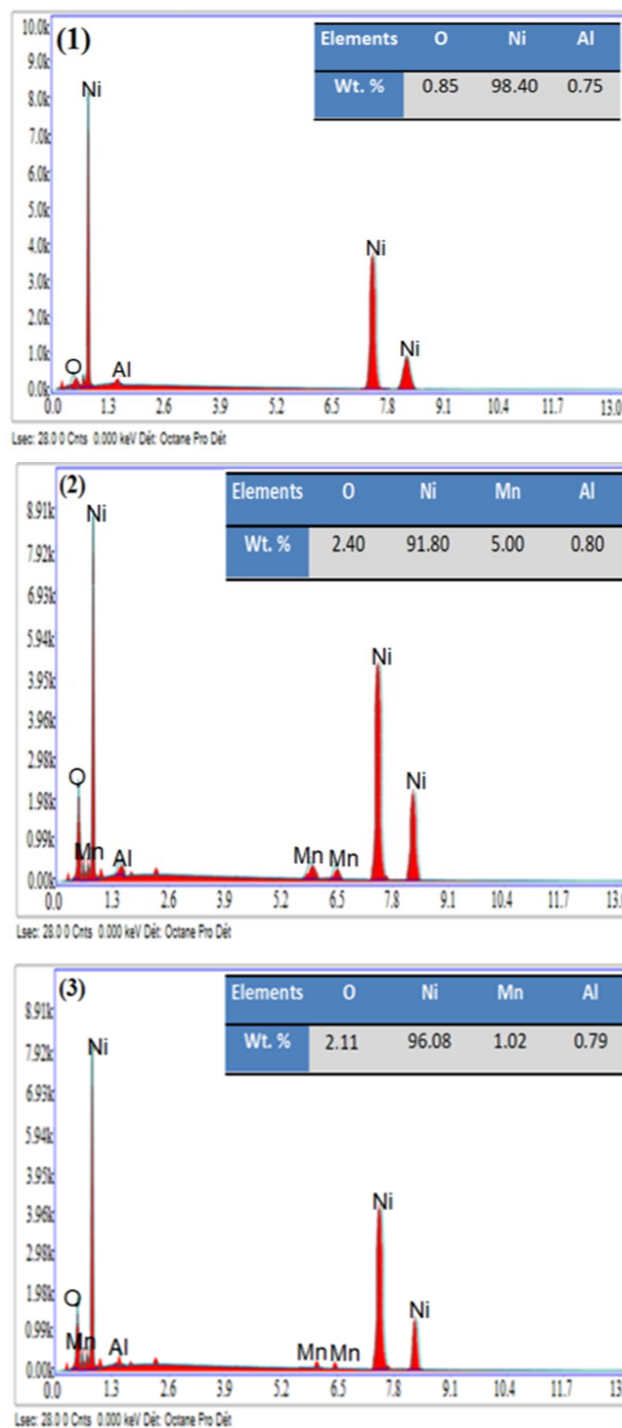


Figure S2. EDX for the reduced samples (1) Ni/Al₂O₃, (2) Ni/Mn_xO_y-Al₂O₃ and (3) Ni/Al₂O₃-Mn_xO_yY.